Contrasting roles of Bi- doping and Bi_2Te_3 alloying on the thermoelectric performance of SnTe

Fudong Zhang[a,#], Xia Qi[a,#], Mingkai He[b], Fengshan Zheng[c], Lei Jin[c,*], Zhanhui Peng[a], Xiaolian Chao[a], Zupei Yang[a,*], Di, Wu[a,*]

[a] Key Laboratory for Macromolecular Science of Shaanxi Province, School of Materials Science and Engineering, Shaanxi Normal University, Xi'an 710062, China.

[b] Department of Physics, The Chinese University of Hong Kong, Hong Kong 999077, China

[c] Ernst Ruska-Centre for Microscopy and Spectroscopy with Electrons Forschungszentrum Jülich GmbH 52428 Jülich, Germany.

[#] These authors contributed equally to this work.

*Correspondence shall be addressed to:

E-mails: l.jin@fz-juelich.de, yangzp@snnu.edu.cn, wud@snnu.edu.cn.

Abstract

Previous studies have revealed that Bi element to be a successful *n*-type dopant in SnTe, and can effectively tune its electronic structure. Nevertheless, the understanding of the role of Bi and Bi_2Te_3 in SnTe seems somewhat confused and simplified, without distinctly distinguishing the relation between the microstructural characters and thermoelectric properties in both cases. Therefore, we try to clarify the roles of Bi- doping and Bi_2Te_3 alloying on the electrical and thermal transport properties in SnTe. We find despite that they both contribute to the valence band convergence of SnTe, Bi_2Te_3 alloying induces little effect on the hole concentration unlike the typical n-type feature of Bi- doping; moreover, Bi_2Te_3 alloying tends to produce dense dislocation arrays at micron-scale grain boundaries which differs significantly from the substitutional point defects character upon Bi- doping. It was then found that Bi_2Te_3 alloying exhibits a relatively higher quality factor ($B \sim \mu_w/\kappa_{lat}$) at higher temperatures than Bi-doping. Subsequent Ge doping in Bi_2Te_3 alloyed samples results in a further valence band convergence and hole concentration optimization, and eventually results in a maximum figure of merit *ZT* of 1.4 at 873 K at the composition of $(Sn_{0.88}Ge_{0.12}Te)_{0.97}$-$(BiTe_{1.5})_{0.03}$.

Introduction

Thermoelectric material owns the capability of directly conversion between electricity and low-grade waste heat, which provides an effective solution to relieve the growing energy crisis and environmental issues [1-3]. The conversion efficiency of a thermoelectric material is usually evaluated by a dimensionless figure of merit defined as $ZT = S^2\sigma T/(\kappa_{lat} + \kappa_{ele})$, where S refers Seebeck coefficient, σ denotes electrical conductivity, T is the absolute temperature, and κ_{ele}, κ_{lat} are the electronic thermal conductivity and lattice thermal conductivity, respectively. Apparently, maximizing the power factor ($S^2\sigma$) and simultaneously minimizing the thermal conductivity ($\kappa = \kappa_{lat} + \kappa_{ele}$) are necessary to achieve a high figure of merit ZT. However, the intrinsic coupling nature among these thermoelectric parameters implies that it is hard to obtain an enhanced ZT value *via* independent modulation of a single parameter [4].

To date, among the numerous thermoelectric materials at intermediate temperatures, including skutterudites [5-6], GeTe [7-8], SnSe [9-10], PbTe [11-12] and its analogue PbSe [13-14] and PbS [15-16] *etc*., of which, PbTe has been regarded as a promising candidate for its good thermal stability, superior mechanical property, and outstanding performance. However, abuse of lead might induce growing worldwide concerns of environmental issues [17]. In the last decade, SnTe has gradually been taken as a natural replacement for PbTe due to its similar crystal and electronic band structures as the latter, although SnTe still faces some intrinsic difficulties as follows [18-19]: (i) the intrinsically high hole concentration (~ 10^{21} cm^{-3}) due to abundant Sn vacancies; (ii) the large energy offset (~ 0.3 eV) between light and heavy valence bands; (iii) the intrinsically high κ_{lat} (~ 3 $Wm^{-1}K^{-1}$ at room temperature). Extensive efforts were thus devoted to overcome these afore-mentioned inferiorities for improved thermoelectric performance. For instance, Mn was reported to be quite effective in modulating the valence bands offset [20-22]. Providing that the solubility of MnTe is very high in GeTe [23], Pei *et al*. [24] successfully increased the solubility (25 mol%) of MnTe in SnTe with the help of 5% GeTe, and realized a significantly enhanced power factor. Doping at Sn site with Cd [25-26], Mg [27], Hg [18], Ca [28], and/or co-doping with Bi/Pb [29], In/Cd [30], In/Ag [31], Ag/Mg [32] were also proved to exhibit a similar function. In addition, indium doping in SnTe was found able to induce resonant levels near valence band maximum (VBM) that is believed to be responsible for the extraordinarily large S [32-33]. Moreover, constructing microstructural defects, like point defect

[22, 34-35], nanostructures [36-39], van der Waals planar defects [40] and hierarchical architecture [41-42], is also able to improve the overall figure of merit from the aspect of reducing lattice thermal conductivity.

Among the mentioned strategies, the *n*-type Bi- doping can simultaneously modulate the valence band offset for an enhanced density of state (DOS) effective mass and strengthen the point defect scattering for a reduced lattice thermal conductivity. In this work, we found that Bi_2Te_3 alloying in SnTe plays quite a different function as Bi-doping mainly in the aspects of charge carrier modulation and phonon scattering mechanism, and exhibits a substantially higher quality factor ($B \sim \mu_w / \kappa_{lat}$) at 773 K. A follow-up Ge doping at Sn site in the optimized Bi_2Te_3 alloyed sample provides a further tuning on hole concentration and valence band alignment, and results in a maximum *ZT* of 1.4 at 873 K at the composition of $(Sn_{0.88}Ge_{0.12}Te)_{0.97}$-$(BiTe_{1.5})_{0.03}$.

Experimental

Material synthesis

High-purity Sn shots (Alfa Aesar, 99.99%), Te chunks (Aladdin, 99.999%), Bi shots (Aladdin, 99.999%) and Ge shots (Aladdin, 99.99%) were weighed according to the nominal compositions and then sealed in quartz tubes under a vacuum of 10^{-4} Pa. Subsequently, the sealed materials were heated in a furnace; the temperature was slowly raised to 673 K within 200 min, then dwelled for 240 min, after which the ampoules were further heated to 1173 K at a speed of 1 K/min, soaked for 720 min here and quenched in cool water. Finally, obtained ingots were hand-ground into fine powders, and followed by spark plasma sintering (LABOX-212, Japan) at 773 K for 5 min under a uniaxial pressure of ~ 50 MPa.

Structure characterizations

The crystal structures of the specimens were characterized by X-ray diffractometer (MiniFlex600, Rigaku, Tokyo, Japan) at a scanning rate of 10° min^{-1} from $2\theta = 20^{\circ}$ to 80°. The microstructures were observed by transmission electron microscopy (TEM) (Thermo Fisher Talos F200X microscope) operated at 200 kV.

Thermoelectric property characterizations

The ZEM-3 apparatus (Ulvac-Riko, Japan) was used to measure the Seebeck coefficient *S* and the electrical conductivity σ at a helium atmosphere. The uncertainties of the *S* and σ are

both estimated to be about 5%. The thermal diffusivity (D) was obtained by the LFA-457 (Netzsch, Germany) laser flash apparatus. The total thermal conductivity κ was calculated according to $\kappa = DC_p\rho$, where ρ is mass density of the sample measured using the Archimedes method (Mettler Toledo, Model XSE105DU), C_p is the heat capacity which was estimated by a theoretical Dulong-Petit limit. The uncertainty of thermal conductivity was estimated to be about 8%. Considering the uncertainties of all the parameters, the uncertainty of calculated ZT is about 15%. Room-temperature n_H and carrier mobility (μ_H) of all samples were measured by a Hall system (Lake Shore 8400 Series, Model 8404, USA), whose uncertainty being about 10%.

Results and discussion

Figure 1a and c show the room temperature X-ray diffraction patterns of as-synthesized $Sn_{1-x}Bi_xTe$ (x = 0, 0.01, 0.03, 0.05) and $Sn_{1-y}Bi_yTe_{1+0.5y}$ (y = 0, 0.01, 0.03, 0.05) samples. In both cases, the main diffraction peaks match well with the cubic rock-salt crystal structure of SnTe ($Fm\bar{3}m$). Weak diffraction peaks corresponding to a secondary Bi phase were observed in Bi-doped samples as $x \geq 0.03$, while Bi_2Te_3 alloyed samples retain single cubic phase all the way from y = 0.01 to 0.05. The calculated lattice parameter of Bi-doped samples, as shown in figure 1b, increases with Bi doping ratio x but quickly saturates at x = 0.03, due to the relatively smaller Sn^{2+} (0.93 Å) ionic radii than Bi^{3+}(0.96 Å). The very small solubility limit of Bi in SnTe was also reported in literature [43]. In contrast, the lattice parameter for Bi_2Te_3 alloyed $Sn_{1-y}Bi_yTe_{1+0.5y}$ family gradually increases till y = 0.03 and starts to drop thereafter (see supporting information figure S1 for XRD patterns of y > 0.05). This unusual behavior of calculated lattice parameter with Bi_2Te_3 alloying ratio y may be attributed to a compensation between the expanding trend due to Bi/Sn substitution and the shrinking trend as the number of cation vacancies grows [44]. The Bi- doped and Bi_2Te_3 alloyed in SnTe can be expressed as Eqn. (1) and (2), respectively. And the corresponding scheme of the process that Bi- doped and Bi_2Te_3 alloyed in SnTe as shown in figure 1e.

$$Bi + SnTe \rightarrow Bi^{\cdot}_{Sn} + e' + Te_{Te} \quad (1)$$

$$Bi_2Te_3 + SnTe \rightarrow 2/3\ Bi^{\cdot}_{Sn} + 1/3\ V''_{Sn} + Te_{Te} \quad (2)$$

In brief, our XRD results revealed that there is obvious difference in lattice configuration

between Bi- doped and Bi_2Te_3 alloyed SnTe samples.

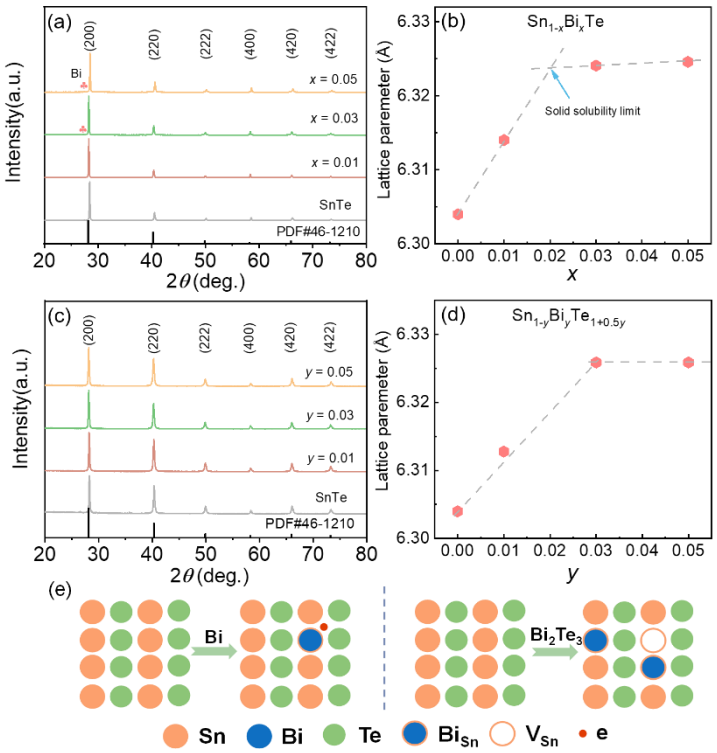

Figure 1 (a) (c) The powder XRD patterns for $Sn_{1-x}Bi_xTe$ (x = 0, 0.01, 0.03, 0.05) and $Sn_{1-y}Bi_yTe_{1+0.5y}$ (y = 0, 0.01, 0.03, 0.05). (b) (d) Calculated lattice parameters obtained from (a) and (c), respectively. (e) The scheme of the process that Bi- doped and Bi_2Te_3 alloyed in SnTe.

In **Figure 2** we present the thermoelectric properties comparison between Bi- doped $Sn_{1-x}Bi_xTe$ and Bi_2Te_3 alloyed $Sn_{1-y}Bi_yTe_{1+0.5y}$ series. As shown in figure 2a, the electrical conductivity for both series decreases monotonically with increasing temperature, manifesting a typical degenerated semiconductor feature. In addition, σ decreases with increasing Bi-doping ratio x, as it does in Bi_2Te_3 alloyed samples; nevertheless, the underlying mechanisms are quite different in these two cases. For Bi- doped $Sn_{1-x}Bi_xTe$ series, the Hall carrier concentration (as seen in figure S2a) decreases markedly as Bi concentration increases, which can be attributed to the neutralization of Sn vacancies upon Bi doping according to Eqn. (1). In the meanwhile, measured carrier mobility decreases because Bi substituting Sn also introduces Bi_{Sn} point defects and Bi-rich nanoparticles, both contributing negatively to the charge carrier mobility. This mechanism was also revealed by Zhou *et al.* [45]. Therefore, in the case of $Sn_{1-x}Bi_xTe$ family, the reduction of σ comes from simultaneous decrease carrier concentration and carrier mobility. In contrast, room temperature Hall measurements reveal that hole

concentration barely changes when Bi_2Te_3 is alloyed into SnTe as in $Sn_{1-y}Bi_yTe_{1+0.5y}$ series, as shown in figure S2b; the decreasing σ with Bi_2Te_3 alloying ratio in $Sn_{1-y}Bi_yTe_{1+0.5y}$ samples then comes solely from the obvious reduction of carrier mobility. The nearly unaltered carrier concentration and decreased carrier mobility could be related to the growing "neutral" cation vacancies upon Bi_2Te_3 alloying [40]. Seebeck coefficients S in both series exhibit an opposite trend with electrical conductivity σ as expected, figure 2b. A Pisarenko plot using two band kane (TBK) model [38] is presented to help analyze the valence band configuration upon Bi-doping and Bi_2Te_3 alloying, figure 2c. Previously reported experimental results of undoped [46] and Bi- doped SnTe [45] are also plotted in the figure as references. As shown, pristine (undoped) SnTe data are well located on the calculated Pisarenko curve with a light-heavy valence band separation $\Delta E_{L\text{-}\Sigma} = 0.35$ eV, indicating the validity of our TBK model. As Bi is doped into SnTe matrix, the experimental S versus n_H points then deviate gradually off the Pisarenko curve with $\Delta E_{L\text{-}\Sigma} = 0.35$ eV and approaching the one with $\Delta E_{L\text{-}\Sigma} = 0.10$ eV, suggesting that Bi- doping in SnTe could produce a valence band convergence as also revealed by Zhou *et al*. [45]. As for Bi_2Te_3 alloying into SnTe, a similar valence band convergence behavior was also suggested as seen in figure 2c. In both cases, the valence band convergence leads to enhanced density-of-state (DOS) effective mass, explaining the large Seebeck coefficient values but also resulting in the reduction of carrier mobility as observed. Eventually, the substantially enhanced S well compensates the reduction of σ, yielding an overall improved PF in the entire temperature range as shown in figure S3a.

The total thermal conductivity (κ) versus temperature for $Sn_{1-x}Bi_xTe$ and $Sn_{1-y}Bi_yTe_{1+0.5y}$ are outlined in figure 2d. The electrical contribution to thermal conductivity κ_{ele} is evaluated by the Wiedemann-Franz law $\kappa_{ele} = L\sigma T$ [47] (L is the Lorenz number which can be approximately derived from S [48]) and shown in figure S3b. Subtracting κ_{ele} from κ gives the lattice thermal conductivity κ_{lat} as displayed in figure 2e. Although both Bi- doping and Bi_2Te_3 alloying result in a considerable reduction of lattice thermal conductivity at lower temperatures ($T < 500$ K), Bi_2Te_3 alloyed samples exhibit relatively lower κ_{lat} values than Bi- doped ones at higher temperatures ($T > 550$ K). For instance, κ_{lat} for $Sn_{0.97}Bi_{0.03}Te_{1.015}$ gets down to 0.83 $Wm^{-1}K^{-1}$ at ~ 723 K while pristine SnTe is as high as ~ 0.93 $Wm^{-1}K^{-1}$ at ~ 723 K. The difference of lattice thermal conductivity at higher temperature between Bi- doped and Bi_2Te_3 alloyed samples can

be explained in two aspects: (i) the reduced hole concentration due to Bi- doping aggravates the bipolar conduction in the narrow-gap SnTe (0.18 eV at 300 K [49]); (ii) Bi- doping strengthens phonon scattering mainly *via* Bi/Sn substitutional point defects and Bi-rich nano-precipitates [45], while Bi_2Te_3 alloying in this work generates dense dislocation arrays at grain boundaries as will be discussed later. The advance of Bi_2Te_3 alloyed samples $Sn_{1-y}Bi_yTe_{1+0.5y}$ over Bi- doped $Sn_{1-x}Bi_xTe$ samples could be further understood by comparing their corresponding quality factors B ($\sim\mu_w/\kappa_{lat}$) [50], where the temperature-dependent weighted mobility (μ_w) was derived from the experimental electrical conductivity σ and Seebeck coefficient S [50] (as shown in figure S3c). As shown in figure 2f, despite that the μ_w /κ_{lat} value of $Sn_{1-y}Bi_yTe_{1+0.5y}$ samples at 323 K is systematically lower than that of $Sn_{1-x}Bi_xTe$ samples, the condition confronts a reversal at 773 K suggesting that a higher overall figure of merit *ZT* shall be realized in the former samples. Indeed, thermoelectric characterizations demonstrates that Bi_2Te_3 alloyed $Sn_{1-y}Bi_yTe_{1+0.5y}$ samples exhibit consistently higher peak *ZT* at 773 K than Bi-doped $Sn_{1-x}Bi_xTe$ ones, as seen in figure S3d, a maximal *ZT* value of 0.75 was realized at 773 K in the composition of $Sn_{0.97}Bi_{0.03}Te_{1.015}$ sample with $y = 0.03$.

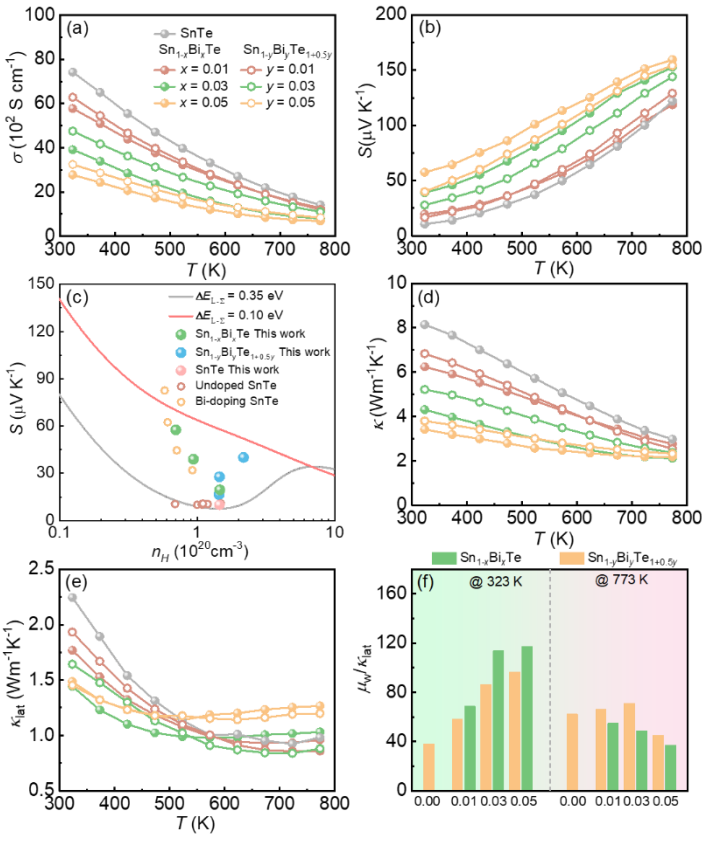

Figure 2 Temperature variation of thermoelectric properties for $Sn_{1-x}Bi_xTe$ (x = 0, 0.01, 0.03, 0.05) and Sn_{1-}

$_y$Bi$_y$Te$_{1+0.5y}$ (y = 0, 0.01, 0.03, 0.05) samples. (a) Electrical conductivity; (b) Seebeck coefficient. (c) Seebeck coefficient as a function of carrier concentration (n_H) versus Pisarenko plots according to the TBK model with a band offset of 0.35 eV and 0.10 eV respectively. (d) Total thermal conductivity; (e) lattice thermal conductivity. (f) The ratio of weighted carrier mobility to lattice thermal conductivity (μ_w /κ_{lat}) at 323K and 773 K, respectively, the unit of μ_w /κ_{lat} is (cm^2 V^{-1}s^{-1}) / (Wm^{-1}K^{-1}).

Transmission electron microscopy (TEM) and scanning transmission electron microscopy (STEM) were used to investigate the microstructural characters of the $Sn_{0.97}Bi_{0.03}Te_{1.015}$ sample. Low-magnification TEM images as shown in **Figure 3**a-b reveal very dense dislocation arrays located at micron-sized grain boundaries, suggesting that lattice mismatching across a grain boundary is of the low-angle feature. These dislocation arrays at low-angle grain boundaries exhibit discriminately scattering efficiency for charge carrier and heat-carrying phonons, thus are beneficial for the decoupling of electron-phonon transports and the overall thermoelectric performance [51-53]. Further STEM images (figure 3c-d) show that the $Sn_{0.97}Bi_{0.03}Te_{1.015}$ sample is physically homogeneous in grains and across grains with Z-contrast, and following energy dispersive spectroscopy (EDS, figure 3e-h) confirms that elements (Bi, Sn and Te) are evenly distributed all over. The combined microstructural characters of homogeneous element distribution and dense dislocation arrays at grain boundaries are believed to be the origin of superior B factor (~μ_w/κ_{lat}) at 773 K in Bi_2Te_3 alloyed $Sn_{1-y}Bi_yTe_{1+0.5y}$ samples.

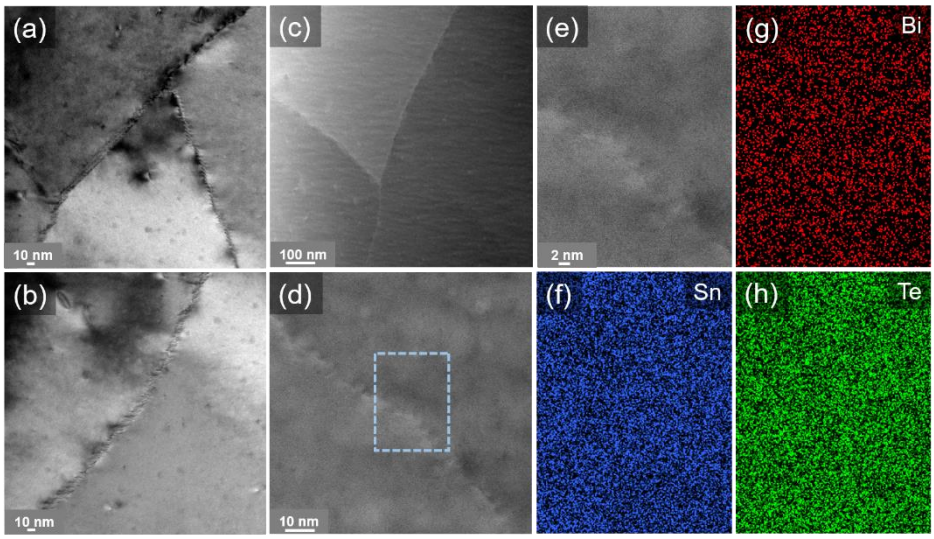

Figure 3 S/TEM analyses of the $Sn_{0.97}Bi_{0.03}Te_{1.015}$ sample. (a) and (b) Low magnification TEM image of $Sn_{0.97}Bi_{0.03}Te_{1.015}$ sample. (c) STEM image showing the grain boundary structure. (d) STEM image of dislocation arrays. (e) Enlarged view obtained of rectangular region shown in from (d), and corresponding EDS elemental maps

of (f) Sn, (g) Bi, and (h) Te.

It is gratifying that Ge alloying in $Sn_{1-x}Ge_xTe$ could obtaine ultralow κ_{lat} by inducing ferroelectric instability near room temperature [54], we achieved in this work an optimal thermoelectric performance based on $Sn_{0.97}Bi_{0.03}Te_{1.015}$ composition (written as $(SnTe)_{0.97}(BiTe_{1.5})_{0.03}$ hereafter) by Ge alloying, due to combined effects of the highly converged valence band and ultralow κ_{lat} as discussed below.

The powder X-ray diffraction (XRD) patterns of $(Sn_{1-z}Ge_zTe)_{0.97}(BiTe_{1.5})_{0.03}$ (z = 0, 0.04, 0.08, 0.12 and 0.15) are shown in figure S5a. As shown, all diffraction peak indexed to the cubic rock salt crystal structure of SnTe ($Fm\bar{3}m$), and no secondary phase observed within detecting limitation of XRD instrument. The calculated lattice parameter (figure S5b) decreases almost linearly with the increasing amount of Ge concentration, demonstrating that smaller atomic radii of Ge (0.87 Å) successfully substitute on the Sn (0.93 Å) site in the face centered cubic SnTe structure.

Figure 4 presents the thermoelectric properties for $(Sn_{1-z}Ge_zTe)_{0.97}(BiTe_{1.5})_{0.03}$ (z = 0, 0.04, 0.08, 0.12 and 0.15) samples. The temperature dependence of σ manifests a degenerate semiconducting behavior, as shown in figure 4a. σ slightly decreases as increasing Ge concentration for the whole temperature range. Specifically, the values of σ at 323 K gradually decreases from ~ 4755 Scm^{-1} for $(SnTe)_{0.97}(BiTe_{1.5})_{0.03}$ to ~ 3880 Scm^{-1} for $(Sn_{0.85}Ge_{0.15}Te)_{0.97}(BiTe_{1.5})_{0.03}$. The reduction of σ mainly arise from the decrease in carrier concentration caused by progressive substitution of Sn by Ge fills the Sn vacancies as shown Meanwhile, the room temperature carrier mobility (figure S6) shows an obvious upward trend with increases amount of Ge, which possibly due to the diminished scattering rate caused by the reduced carrier concentration. It is interestingly noted that the high value of carrier mobility in $Sn_{1-x}Ge_xTe$ was ascribed to a dielectric screening effect by Banik *et al*. [54] Seebeck coefficient S gets gradually enhanced with Ge content, corresponding well to the variation of carrier concentration, as shown in figure 4b. The combination of substantially enhanced S with optimal carrier concentration eventually yields an enhanced PF plateaus over a broad temperature range. As shown in figure 4c, the value of PF at 323 K is ~ 8.2 $\mu Wcm^{-1}K^{-2}$ for $(Sn_{0.88}Ge_{0.12}Te)_{0.97}(BiTe_{1.5})_{0.03}$ sample, and further rises with increasing temperature to ~ 32 $\mu Wcm^{-1}K^{-2}$ at 873 K. Total thermal conductivity κ decreases with increasing amounts of Ge,

from ~ 5.21 $Wm^{-1}K^{-1}$ in $(SnTe)_{0.97}(BiTe_{1.5})_{0.03}$ drop to ~ 4.21 $Wm^{-1}K^{-1}$ in $(Sn_{0.88}Ge_{0.12}Te)_{0.97}(BiTe_{1.5})_{0.03}$ at 323 K, as shown figure 4d. After subtracting the electrical contribution, the calculated lattice thermal conductivity κ_{lat} experiences drastic reduction upon Ge substitution over the entire temperature range of our measurements (323-873 K), as shown in figure 4e. Specifically, κ_{lat} at 323 K significantly decrease from ~ 1.68 $Wm^{-1}K^{-1}$ for pristine $(SnTe)_{0.97}(BiTe_{1.5})_{0.03}$ to ~ 1.12 $Wm^{-1}K^{-1}$ for $(Sn_{0.96}Ge_{0.04}Te)_{0.97}(BiTe_{1.5})_{0.03}$. Noted that the reduction of κ_{lat} is more profound at high temperatures, *e.g.*, minimal κ_{lat} for $(Sn_{0.96}Ge_{0.04}Te)_{0.97}(BiTe_{1.5})_{0.03}$ even drops to 0.39 $Wm^{-1}K^{-1}$ at 673 K. Due to the synergetic effects of reduced thermal conductivity, substantially enhanced *S* and *PF* upon Ge doping, a maximum *ZT* values of 1.4 can then be achieved in the composition of $(Sn_{0.88}Ge_{0.12}Te)_{0.97}(BiTe_{1.5})_{0.03}$ at 873 K as presents in figure 4f.

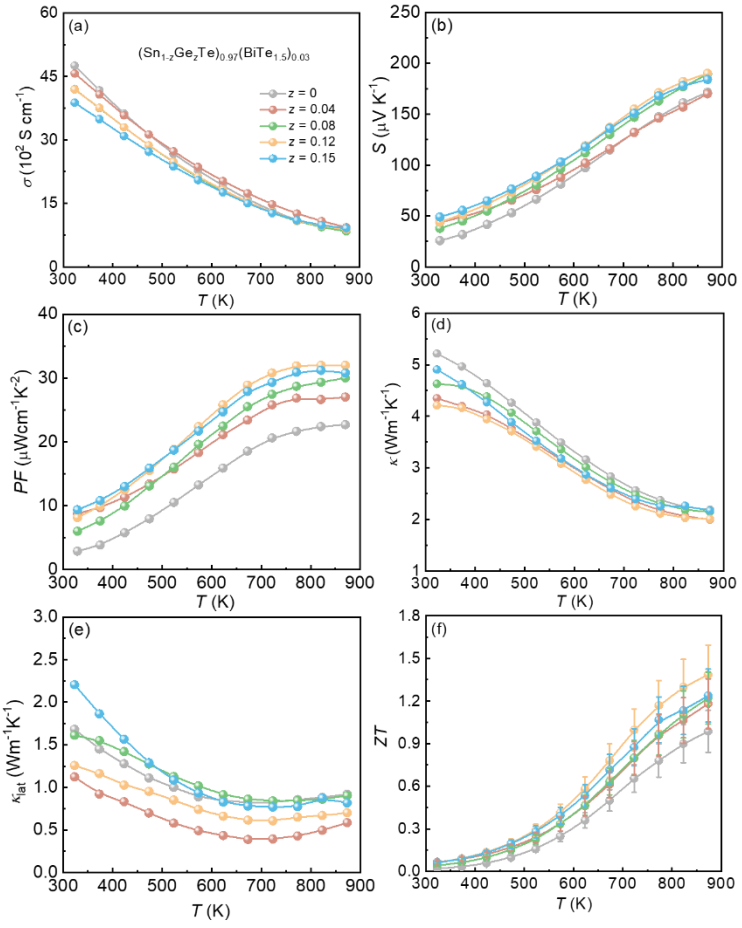

Figure 4 The thermoelectric properties for $(Sn_{1-z}Ge_zTe)_{0.97}$ $(BiTe_{1.5})_{0.03}$ (z = 0, 0.04, 0.08, 0.12 and 0.15) samples. (a) Electrical conductivity; (b) Seebeck coefficient; (c) power factor; (d) total thermal conductivity; (e) lattice thermal conductivity; (e) *ZT* values.

Besides, the Ge doping can effectively reduce the lattice thermal conductivity of Bi_2Te_3 alloyed $(SnTe)_{0.97}(BiTe_{1.5})_{0.03}$, we also found that it helps to promote valence bands convergence by fitting experimental data with calculated Pisarenko plot with a TBK model, **Figure 5**a; *S* versus carrier concentration n_H of others SnTe-based series [25, 32, 54-55] were also illustrated. As seen, the band offset between light and heavy valence bands gradually approaches 0.1 eV with increases amount of Ge (as the red arrow shows). Knowing that Bi_2Te_3 alloying also contribute to the valence band convergence, we plotted a schematic figure showing the valence band evolution with Bi_2Te_3 alloying and Ge doping in figure 5b. To have a comprehensive understanding of the merits of our work, we compared the thermoelectric properties of the present work with state-of-art SnTe-based systems [22, 30-31, 37-38, 40-41, 56-57] in figure 5c and d. Among these advanced *p*-type SnTe compositions, our $(Sn_{0.88}Ge_{0.12}Te)_{0.97}(BiTe_{1.5})_{0.03}$ sample shows a competitively high *ZT* value especially at high temperature range shown in figure 5c. The maximum *ZT* values of 1.4 at 873 K and the average ZT_{ave} of ~ 0.61 between 323 K and 873 K are seemingly among the highest ones in all SnTe-based *p*-type thermoelectrics. Evidently, these merits demonstrated the extraordinariness of $(Sn_{0.88}Ge_{0.12}Te)_{0.97}(BiTe_{1.5})_{0.03}$ thermoelectric materials for efficient waste heat recovery and power generation applications at intermediate temperature.

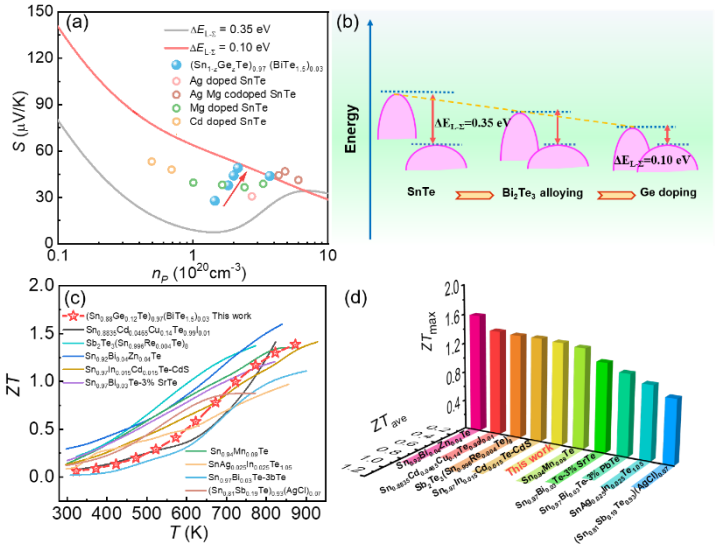

Figure 5 (a) Pisarenko plot with a TBK model showing the band convergence in $(Sn_{1-z}Ge_zTe)_{0.97}(BiTe_{1.5})_{0.03}$ (z = 0, 0.04, 0.08, 0.12 and 0.15). (b) The schematic image of valence band evolution due to Bi_2Te_3 alloying and Ge doping. (c) and (d) The thermoelectric properties for present work as compared with other reported state-of-art SnTe systems

[22, 30-31, 37-38, 40-41, 56-57].

Conclusions

To summarize, we distinguished in this work the contrasting roles of Bi- doping and Bi_2Te_3 alloying in SnTe, which are mainly reflected in two aspects. First, the solubility of Bi- doping in SnTe is far smaller than that of Bi_2Te_3 alloying, coming probably from the difference lattice occupations of Bi atoms in the two cases. Second, the B factors ($\sim\mu_w/\kappa_{lat}$) in Bi_2Te_3 alloyed samples are higher than that in Bi- doped ones at 773 K, originating from the low-angle grain boundary (and dense dislocation arrays thereon) character for the former. Additional Ge doping in 3 mol% Bi_2Te_3 alloyed composition $(SnTe)_{0.97}(BiTe_{1.5})_{0.03}$ leads to a further valence bands convergence and a reduced lattice thermal conductivity, eventually an enhanced thermoelectric performance ($ZT_{max} \approx 1.4$ at 873 K; $ZT_{ave} \approx 0.61$ from 323 - 873 K) in the composition of $(Sn_{0.88}Ge_{0.12}Te)_{0.97}(BiTe_{1.5})_{0.03}$.

Author contributions

F. D. Z. and X. Q. conceptualized the idea and wrote the initial draft of the manuscript. X. Q. and M. K. H. assisted with sample fabrication. F. D. Z., X. Q. and M. K. H. acquired and analyzed the thermoelectric performance data. F. S. Z. and L. J. carried out the TEM/STEM characterization. D. W. designed the project and involved in reviewing and editing this manuscript. Z. H. P., X. L. C., Z. P. Y. and D. W. provided the necessary resources and infrastructure for this work.

Conflicts of interest

There are no conflicts to declare.

Acknowledgments

The authors would like to thank the financial support of the Natural Science Basic Research Plan in the Shaanxi Province of China (Grant Nos. 2021JM-201 and 2021ZDLSF06-03), the National Natural Science Foundation of China (Nos. 51872177 and 51901121), the Fundamental Research Funds for the Central Universities (Program Nos. GK202002014, GK202103022 and 2021TS009), the Science and Technology Project of Xi'an (Grant No.

2020KJRC0014). Supports from Shaanxi Sanqin Scholars Innovation Team were also appreciated.

Notes and references

[1] F. Guo, B. Cui, C. Li, Y. Wang, J. Cao, X. Zhang, Z. Ren, W. Cai, J. Sui, Ultrahigh thermoelectric performance in environmentally friendly SnTe achieved through stress-induced lotus-seedpod-like grain boundaries, *Adv*. *Funct*. *Mater*., 2021, **31**, 2101554.

[2] X. Hu, P. Jood, M. Ohta, M. Kunii, K. Nagase, H. Nishiate, M. G. Kanatzidis, A. Yamamoto, Power generation from nanostructured PbTe-based thermoelectrics: comprehensive development from materials to modules, *Energy Environ*. *Sci*., 2016, **9**, 517-529.

[3] Z. G. Chen, W. D. Liu, Thermoelectric coolers: infinite potentials for finite localized microchip cooling, *J. Mater. Sci. Technol.*, 2022, **121**, 256-262.

[4] T. Zhu, Y. Liu, C. Fu, J. P. Heremans, J. G. Snyder, X. Zhao, Compromise and synergy in high-efficiency thermoelectric materials, *Adv*. *Mater*., 2017, **29**, 1605884.

[5] Z. H. Ge, W. J. Li, J. Feng, F. Zheng, C. L. Jia, D. Wu, L. Jin, Atomic-scale observation of off-centering rattlers in filled skutterudites, *Adv*. *Energy Mater*., 2022, **12**, 2103770.

[6] X. Meng, Z. Liu, B. Cui, D. Qin, H. Geng, W. Cai, L. Fu, J. He, Z. Ren, J. Sui, Grain boundary engineering for achieving high thermoelectric performance in *n*-Type skutterudites, *Adv*. *Energy Mater*., 2017, **7** (13), 1602582.

[7] Z. Bu, X. Zhang, B. Shan, J. Tang, H. Liu, Z. Chen, S. Lin, W. Li, Y. Pei, Realizing a 14% single-leg thermoelectric efficiency in GeTe alloys, *Sci*. *Adv*., 2021, **7**, eabf 2738.

[8] G. Bai, Y. Yu, X. Wu, J. Li, Y. Xie, L. Hu, F. Liu, M. Wuttig, O. Cojocaru-Mirédin, C. Zhang, Boron strengthened GeTe-based alloys for robust thermoelectric devices with high output power density, *Adv*. *Energy Mater*., 2021, **11** (37), 2102012.

[9] D. Wang, L. Su, S. Wang, B. Qin, Y. Wang, Y. Qin, Y. Jin, C. Chang, L. D. Zhao, High thermoelectric performance realized through manipulating layered phonon-electron decoupling, *Science*, 2022, **375**, 1385–1389.

[10] C. Chang, D. Wang, D. He, W. He, F. Zhu, G. Wang, J. He, L. D. Zhao, Realizing high-ranged out-of-plane *ZT*s in *n*-type SnSe crystals through promoting continuous phase

transition, *Adv*. *Energy Mater*., 2019, **9** (28), 1901334.

[11] B. Jia, Y. Huang, Y. Wang, Y. Zhou, X. Zhao, S. Ning, X. Xu, P. Lin, Z. Chen, B. Jiang, J. He, Realizing high thermoelectric performance in non-nanostructured *n*-type PbTe, *Energy Environ*. *Sci*., 2022, **5**, 1920-1929.

[12] Y. Xiao, H. Wu, D. Wang, C. Niu, Y. Pei, Y. Zhang, I. Spanopoulos, I. T. Witting, X. Li, S. J. Pennycook, G. J, Snyder, M. G. Kanatzidis, L. D. Zhao, Amphoteric indium enables carrier engineering to enhance the power factor and thermoelectric performance in *n*-type $Ag_nPb_{100}In_nTe_{100+2n}$(LIST), *Adv*. *Energy Mater*., 2019, **9** (17), 1900414.

[13] Y. Xiao, L. Xu, T. Hong, H. Shi, S. Wang, X. Gao, X. Ding, J. Sun, L. D. Zhao, Ultrahigh carrier mobility contributes to remarkably enhanced thermoelectric performance in n-type PbSe, *Energy Environ*. *Sci*., 2022, **15**, 346-355.

[14] J. Cai, J. Yang, G. Liu, L. Xu, X. Wang, H. Hu, X. Tan, J. Jiang, Boosting the thermoelectric performance of PbSe from the band convergence driven by spin-orbit coupling, *Adv*. *Energy Mater*., 2022, **12**, 2103287.

[15] Y. Xiao, D. Wang, Y. Zhang, C. Chen, S. Zhang, K. Wang, G. Wang, S. J. Pennycook, G. J. Snyder, H. Wu, L. D. Zhao, Band sharpening and band alignment enable high quality factor to enhance thermoelectric performance in *n*-Type PbS, *J*. *Am*. *Chem*. *Soc*., 2020, **142** (8), 4051-4060.

[16] B. Jiang, X. Liu, Q. Wang, J. Cui, B. Jia, Y. Zhu, J. Feng, Y. Qiu, M. Gu, Z. Ge, J. He, Realizing high-efficiency power generation in low-cost PbS-based thermoelectric materials, *Energy Environ*. *Sci*., 2020, **13** (2), 579-591.

[17] L. Zhang, X. L. Shi, Y. L. Yang, Z. G. Chen, Flexible thermoelectric materials and devices: From materials to applications, *Mater. Today*, 2021, **46**, 62-108.

[18] G. Tan, F. Shi, J. W. Doak, H. Sun, L. D. Zhao, P. Wang, C. Uher, C.Wolverton, V. P. Dravid, M. G. Kanatzidis, Extraordinary role of Hg in enhancing the thermoelectric performance of *p*-type SnTe, *Energy Environ*. *Sci*., 2015, **8** (1), 267-277.

[19] R. Moshwan, L. Yang, J. Zou, Z. G. Chen, Eco-friendly SnTe thermoelectric materials: progress and future challenges. *Adv*. *Funct*. *Mater*., 2017, **27** (43), 1703278.

[20] G. Tan, F. Shi, S. Hao, H. Chi, T. P. Bailey, L. D. Zhao, C. Uher, C. Wolverton, V. P. Dravid, M. G. Kanatzidis, Valence band modification and high thermoelectric performance in

SnTe heavily alloyed with MnTe, *J. Am. Chem. Soc*., 2015, **137** (35), 11507-16.

[21] W. Li, Z. Chen, S. Lin, Y. Chang, B. Ge, Y. Chen, Y. Pei, Band and scattering tuning for high performance thermoelectric $Sn_{1-x}Mn_xTe$ alloys, *J. Materiomics*, 2015, **1** (4), 307-315.

[22] F. Guo, B. Cui, Y. Liu, X. Meng, J. Cao, Y. Zhang, R. He, W. Liu, H. Wu, S. J. Pennycook, W. Cai, J. Sui, Dense dislocations, and interstitials through Sn self-compensation and Mn alloying, *Small*, 2018, **14** (37), 1802615.

[23] W. D. Johnston, D. E. Sestrich, The MnTe-GeTe phase diagram, *J. Vnorg. Nucl. Chem.*, 1961, **19**, 229-236

[24] J. Tang, B. Gao, S. Lin, J. Li, Z. Chen, F. Xiong, W. Li, Y. Chen, Y. Pei, Manipulation of band structure and interstitial defects for improving thermoelectric SnTe, *Adv. Funct. Mater*., 2018, **28** (34), 1803586.

[25] G. Tan, L. D. Zhao, F. Shi, J. W. Doak, S. H. Lo, H. Sun, C. Wolverton, V. P. Dravid, C. Uher, M. G. Kanatzidis, High thermoelectric performance of *p*-type SnTe via a synergistic band engineering and nanostructuring approach, *J. Am. Chem. Soc*., 2014, **136** (19), 7006-17.

[26] M. Ibanez, R. Hasler, A. Genc, Y. Liu, B. Kuster, M. Schuster, O. Dobrozhan, D. Cadavid, J. Arbiol, A. Cabot, M. V. Kovalenko, Ligand-mediated band engineering in bottom-up assembled SnTe nanocomposites for thermoelectric energy conversion, *J. Am. Chem*. Soc., 2019, **141** (20), 8025-8029.

[27] A. Banik, U. S. Shenoy, S. Anand, U. V. Waghmare, K. Biswas, Mg alloying in SnTe facilitates valence band convergence and optimizes thermoelectric properties, *Chem. Mater*., 2015, **27** (2), 581-587.

[28] T. Hussain, X. Li, M. H. Danish, M. U. Rehman, J. Zhang, D. Li, G. Chen, G. Tang, Realizing high thermoelectric performance in eco-friendly SnTe via synergistic resonance levels, band convergence and endotaxial nanostructuring with Cu_2Te, *Nano Energy*, 2020, **73**, 104832.

[29] U. S. Shenoy, D. K. Bhat, Improving the *ZT* of SnTe using electronic structure engineering: unusual behavior of Bi dopant in the presence of Pb as a co-dopant, *Mater. Adv*., 2021, **2** 6267-6271.

[30] G. Tan, F. Shi, S. Hao, H. Chi, L. D. Zhao, C. Uher, C. Wolverton, V. P. Dravid, M. G.

Kanatzidis, Codoping in SnTe: enhancement of thermoelectric performance through synergy of resonance levels and band convergence, *J. Am. Chem. Soc.*, 2015, **137** (15), 5100-12.

[31] A. Banik, U. S. Shenoy, S. Saha, U. V. Waghmare, K. Biswas, High power factor and enhanced thermoelectric performance of SnTe-$AgInTe_2$: synergistic effect of resonance level and valence band convergence, *J. Am. Chem. Soc.*, 2016, **138** (39), 13068-13075.

[32] R. Pathak, D. Sarkar, K. Biswas, Enhanced band convergence and ultra-low thermal conductivity lead to high thermoelectric performance in SnTe, *Angew. Chem. Int. Ed.*, 2021, **60** (32), 17686-17692.

[33] Q. Zhang, B. Liao, Y. Lan, K. Lukas, W. Liu, K. Esfarjani, C. Opeil, D. Broido, G. Chen, Z. Ren, High thermoelectric performance by resonant dopant indium in nanostructured SnTe, *Proc. Natl. Acad. Sci.* USA, 2013, **110** (33), 13261-6.

[34] Y. Pei, L. Zheng, W. Li, S. Lin, Z. Chen, Y. Wang, X. Xu, H. Yu, Y. Chen, B. Ge, Interstitial point defect scattering contributing to high thermoelectric performance in SnTe, *Adv. Electron. Mater.*, 2016, **2** (6), 1600019..

[35] H. Pang, Y. Qiu, D. Wang, Y. Qin, R. Huang, Z. Yang, X. Zhang, L. D. Zhao, Realizing *n*-type SnTe thermoelectrics with competitive performance through suppressing Sn vacancies, *J. Am. Chem. Soc.*, 2021, **143** (23), 8538-8542.

[36] A. Banik, B. Vishal, S. Perumal, R. Datta, K. Biswas, The origin of low thermal conductivity in $Sn_{1-x}Sb_xTe$: phonon scattering via layered intergrowth nanostructures, *Energy Environ. Sci.*, 2016, **9** (6), 2011-2019.

[37] L. D. Zhao, X. Zhang, H. Wu, G. Tan, Y. Pei, Y. Xiao, C. Chang, D. Wu, H. Chi, L. Zheng, S. Gong, C. Uher, J. He, M. G. Kanatzidis, Enhanced thermoelectric properties in the counter-doped SnTe system with strained endotaxial SrTe, *J. Am. Chem. Soc.*, 2016, **138** (7), 2366-73.

[38] X. Qi, Y. Huang, D. Wu, B. Jiang, B. Zhu, X. Xu, J. Feng, B. Jia, Z. Shu, J. He, Eutectoid nano-precipitates inducing remarkably enhanced thermoelectric performance in $(Sn_{1-x}Cd_xTe)_{1-y}(Cu_2Te)_y$, *J. Mater. Chem. A*, 2020, **8** (5), 2798-2808.

[39] Z. Ma, C. Wang, J. Lei, Zhang, Y. Chen, Y. Wang, J. Wang, Z. Cheng, Core-shell nanostructures introduce multiple potential barriers to enhance energy filtering for the

improvement of the thermoelectric properties of SnTe, *Nanoscale*, 2020, **12** (3), 1904-1911.

[40] X. Xu, J. Cui, Y. Yu, B. Zhu, Y. Huang, L. Xie, D. Wu, J. He, Constructing van der Waals gaps in cubic-structured SnTe-based thermoelectric materials, *Energy Environ*. *Sci*., 2020, **13**, 5135-5142..

[41] X. Zhang, D. Wang, H. Wu, M. Yin, Y. Pei, S. Gong, L. Huang, S. J. Pennycook, J. He, L. D. Zhao, Simultaneously enhancing the power factor and reducing the thermal conductivity of SnTe via introducing its analogues, *Energy Environ*. *Sci*., 2017, **10** (11), 2420-2431.

[42] J. Wang, Y. Yu, J. He, J. Wang, B. Ma, X. Chao, Z. Yang, D. Wu, Synergy of valence band modulation and grain boundary engineering leading to improved thermoelectric performance in SnTe, *ACS Appl*. *Energy Mater*., 2021, **4** (12), 14608-14617.

[43] A. A. T. K. Adouby, G. Kra, J. Olivier-Fourcade, J. C. Jumas, C. P. Vicente, Phase diagram and local environment of Sn and Te: SnTe-Bi and SnTe-Bi_2Te_3 systems, *C. R. Acad. Sci., Ser. IIc: Chim.*, 2000, **3**, 51-58.

[44] Q. Yang, T. Lyu, Z. Li, H. Mi, Y. Dong, H. Zheng, Z. Sun, W. Feng, G. Xu, Realizing widespread resonance effects to enhance thermoelectric performance of SnTe, *J. Alloys Compd.*, 2021, **852**, 156989.

[45] Z. Zhou, J. Yang, Q. Jiang, Y. Luo, D. Zhang, Y. Ren, X. He, J. Xin, Multiple effects of Bi doping in enhancing the thermoelectric properties of SnTe, *J. Mater*. *Chem*. A, 2016, **4** (34), 13171-13175.

[46] R. F. Brebrick, Deviations from stoichiometry and electrical properties in SnTe, *J. Phys*. *Chem*. *Solid*., 1963, **24** (1), 27-36.

[47] R. Moshwan, W. D. Liu, X. L. Shi, Y. P. Wang, J. Zou, Z. G. Chen, Realizing high thermoelectric properties of SnTe via synergistic band engineering and structure engineering, *Nano Energy*, 2019, **65**, 104056.

[48] H. S. Kim, Z. M. Gibbs, Y. Tang, H. Wang, G. J. Snyder, Characterization of Lorenz number with Seebeck coefficient measurement, *APL Mater*., 2015, **3** (4), 041506.

[49] X. Li, J. Liu, S. Li, J. Zhang, D. Li, R. Xu, Q. Zhang, X. Zhang, B. Xu, Y. Zhang, F. Xu, G. Tang, Synergistic band convergence and endotaxial nanostructuring: achieving ultralow

lattice thermal conductivity and high figure of merit in eco-friendly SnTe, *Nano Energy*, 2020, **67**, 104261.

[50] G. J. Snyder, A. H. Snyder, M. Wood, R. Gurunathan, B. H. Snyder, C. Niu, Weighted mobility, *Adv. Mater.*, 2020, **32** (25), 2001537.

[51] D. Wu, X. Chen, F. Zheng, H. Du, L. Jin, R. E. Dunin-Borkowski, Dislocation evolution and migration at grain boundaries in thermoelectric SnTe, *ACS Appl. Energy Mater.*, 2019, **2** (4), 2392-2397.

[52] J. Y. Hwang, J. Kim, H. S. Kim, S. Kim, K. H. Lee, S. W. Kim, Effect of dislocation arrays at grain boundaries on electronic transport properties of bismuth antimony telluride: unified strategy for high thermoelectric performance, *Adv. Energy Mater.*, 2018, **8** (20), 1800065.

[53] F. Zhang, D. Wu, J. He, The roles of grain boundaries in thermoelectric transports, *Materials Lab*, 2022, **1**, 220012.

[54] A. Banik, T. Ghosh, R. Arora, M. Dutta, J. Pandey, S. Acharya, A. Soni, U. V. Waghmare, K. Biswas, Engineering ferroelectric instability to achieve ultralow thermal conductivity and high thermoelectric performance in $Sn_{1-x}Ge_xTe$, *Energy Environ. Sci.*, 2019, **12** (2), 589-595.

[55] D. Sarkar, T. Ghosh, A. Banik, S. Roychowdhury, D. Sanyal, K. Biswas, Highly converged valence bands and ultralow lattice thermal conductivity for high-performance SnTe thermoelectrics, *Angew. Chem. Int. Ed.*, 2020, **59** (27), 11115-11122.

[56] U. S. Shenoy, D. K. Bhat, Bi and Zn co-doped SnTe thermoelectrics: interplay of resonance levels and heavy hole band dominance leading to enhanced performance and a record high room temperature *ZT*, *J. Mater. Chem. C*, 2020, **8** (6), 2036-2042.

[57] X. Dong, W. Cui, W. D. Liu, S. Zheng, L. Gao, L. Yue, Y. Wu, B. Wang, Z. Zhang, L. Chen, Z. G. Chen, Synergistic band convergence and defect engineering boost thermoelectric performance of SnTe, *J. Mater. Sci. Technol.*, 2021, **86**, 204-209.